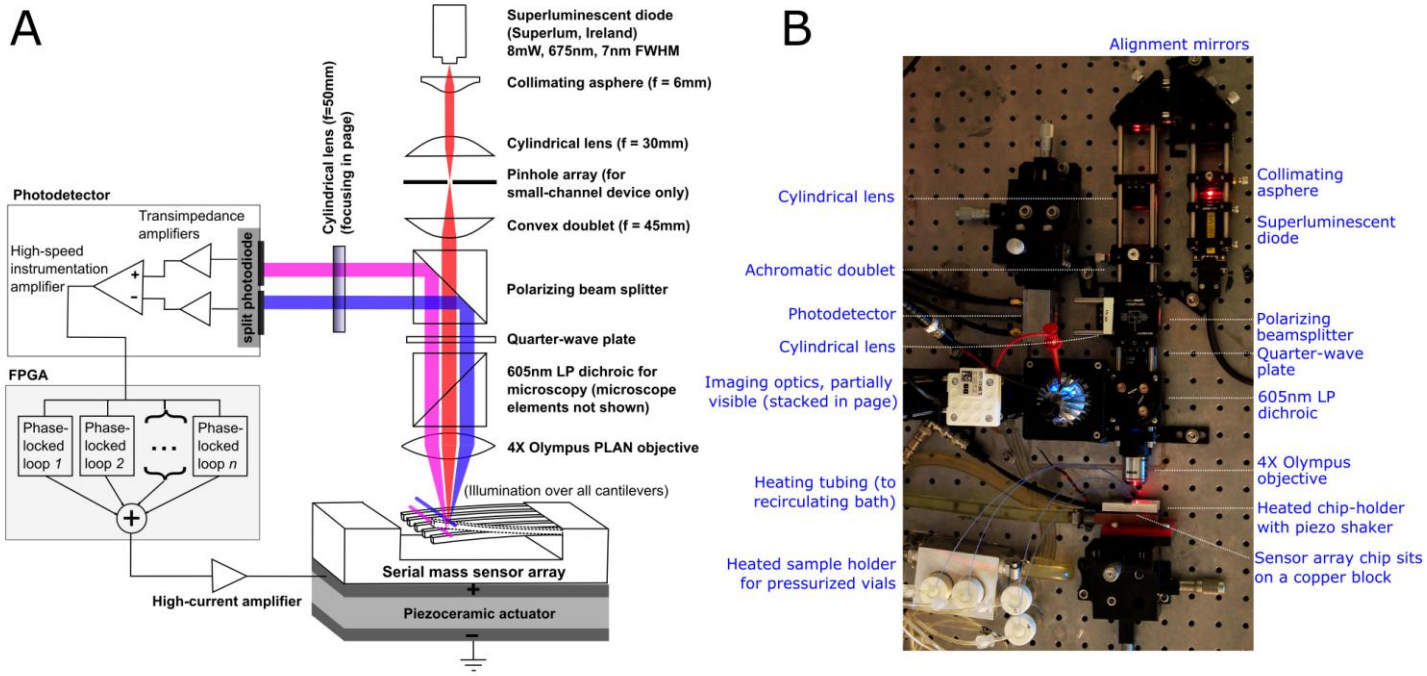

Supplementary Figure 1

Schematic of the control system for the serial microfluidic mass sensor array.

(A) Schematic of optical and electronic path of parallel feedback loops for each mass sensor. (B) Photograph of the optical setup implementing the schematic in (A). The photograph shows the sample holder and the fluidic connections to the sensor chip.

Nature Biotechnology: doi:10.1038/nbt.3666

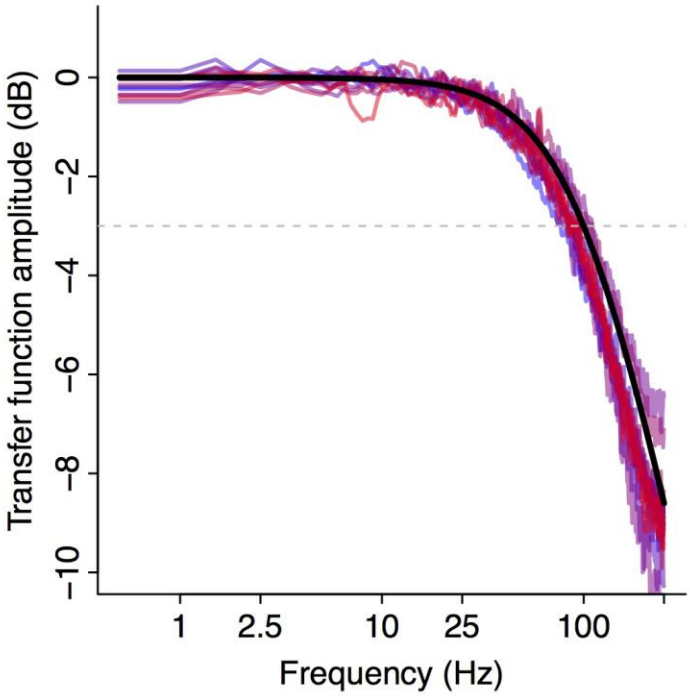

Supplementary Figure 2

Transfer functions of the PLL–cantilever control loops.

Measured transfer functions (colored lines) of all twelve PLL-cantilever feedback loops on a single large-channel serial SMR device. Bandwidth had been set to 100 Hz according to the method in [1]. Solid black line shows ideal 100 Hz first-order response, dashed grey line indicates -3 dB bandwidth.

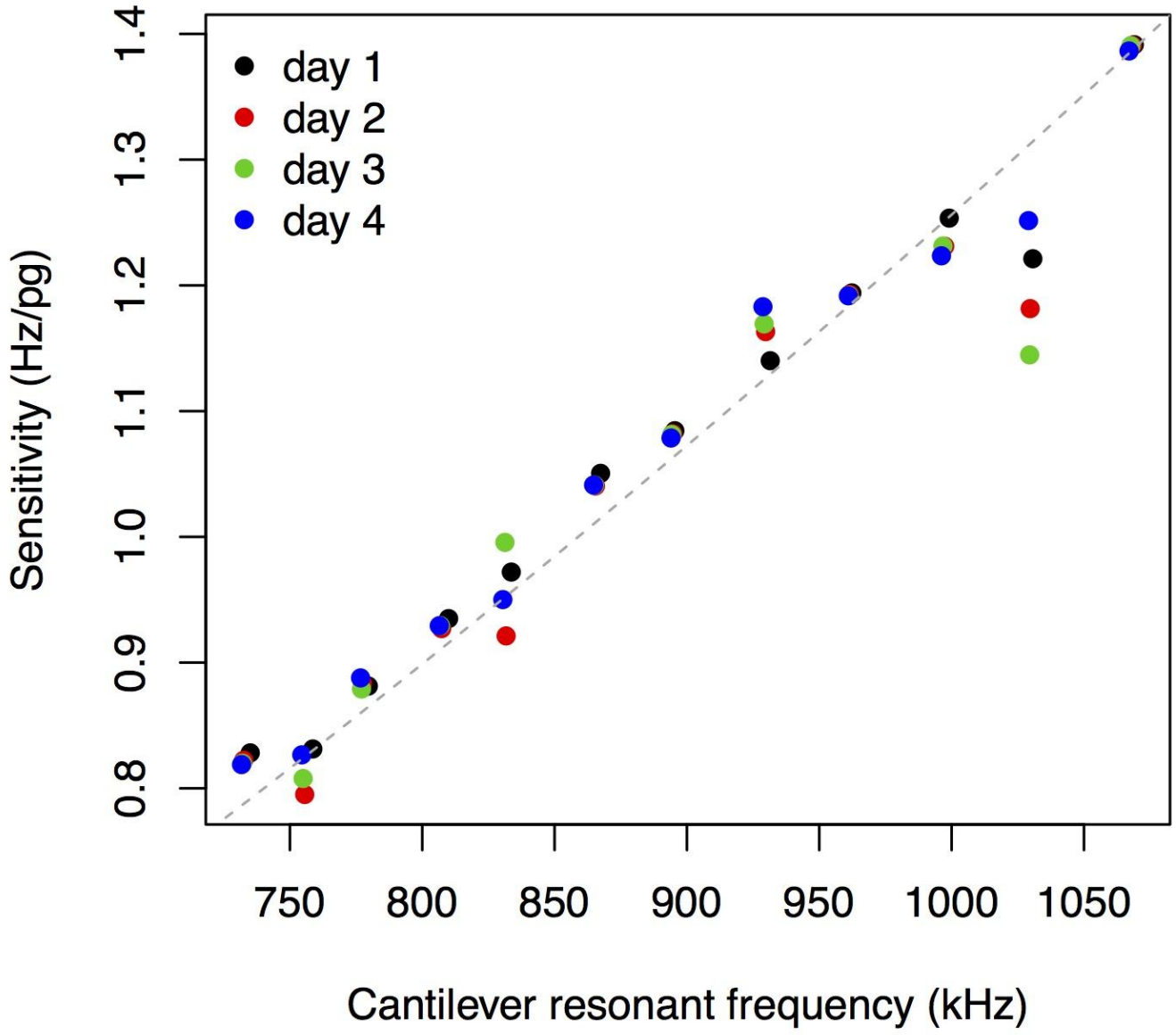

Supplementary Figure 3

Sensitivities of the mass sensors in a large-channel device.

Resonant frequency versus mass sensitivity for a single large-channel device, measured daily during the mouse CD8 cell experiments (Figure 3 in the main text). Dashed grey line shows best fit of data to $y = ax^{1.5}$, illustrating how sensitivity scales with frequency to the power of 1.5. While fabrication tolerances and slight variations in geometry may explain some of the deviations from the model, it remains unclear why some cantilevers exhibit substantial day-to-day variation.

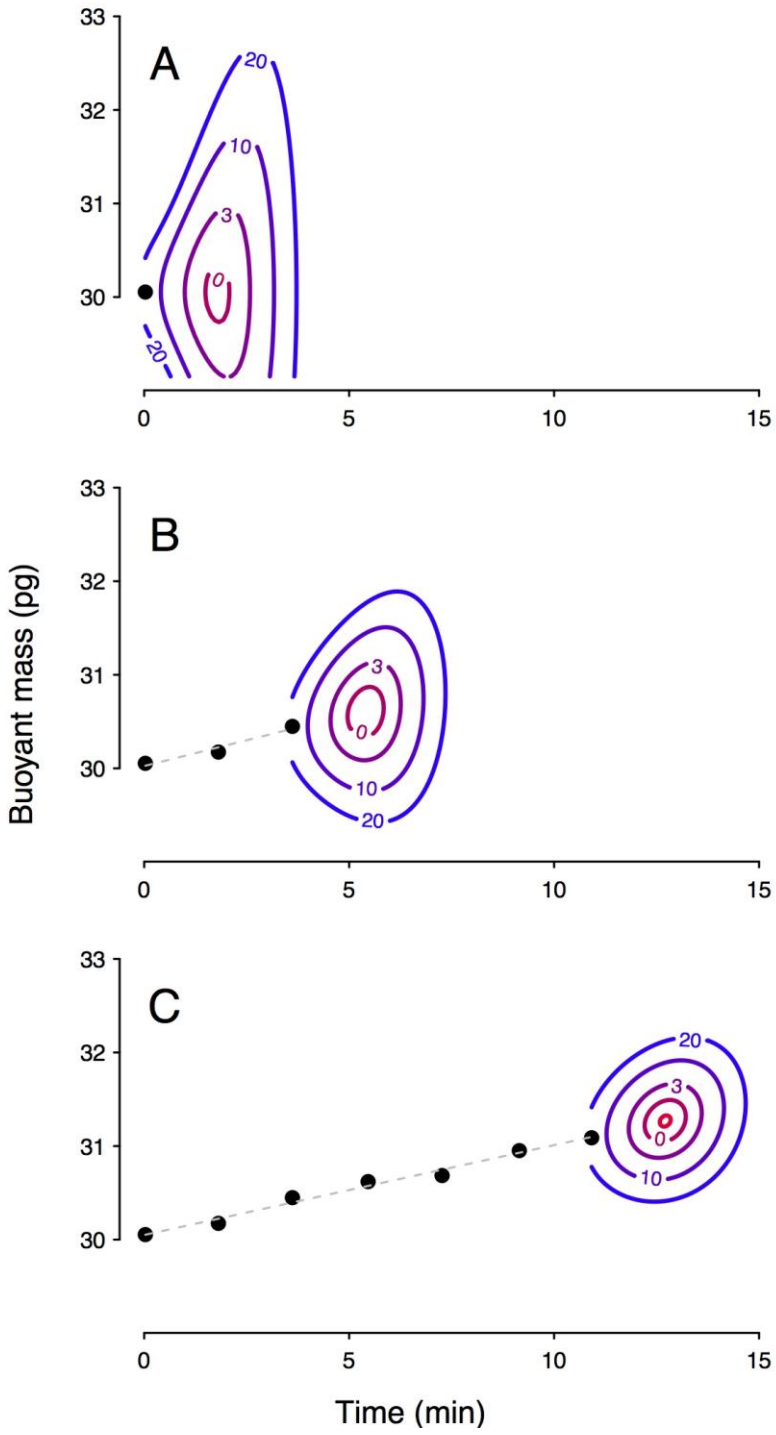

Supplementary Figure 4

Example contour plots of the cost function used in the matching algorithm.

Contour plots of the cost function for several simulated example cells with varying numbers of previous peaks observed (black points). (A) If a cell only has a single peak assigned, the cost function is shaped like a wide bowl, shaped almost entirely by the prior assumptions on mass accumulation rate and system noise. (B), (C) As more data points are observed, the mass accumulation rate becomes established and the cost function contours become determined by the system's mass measurement noise.

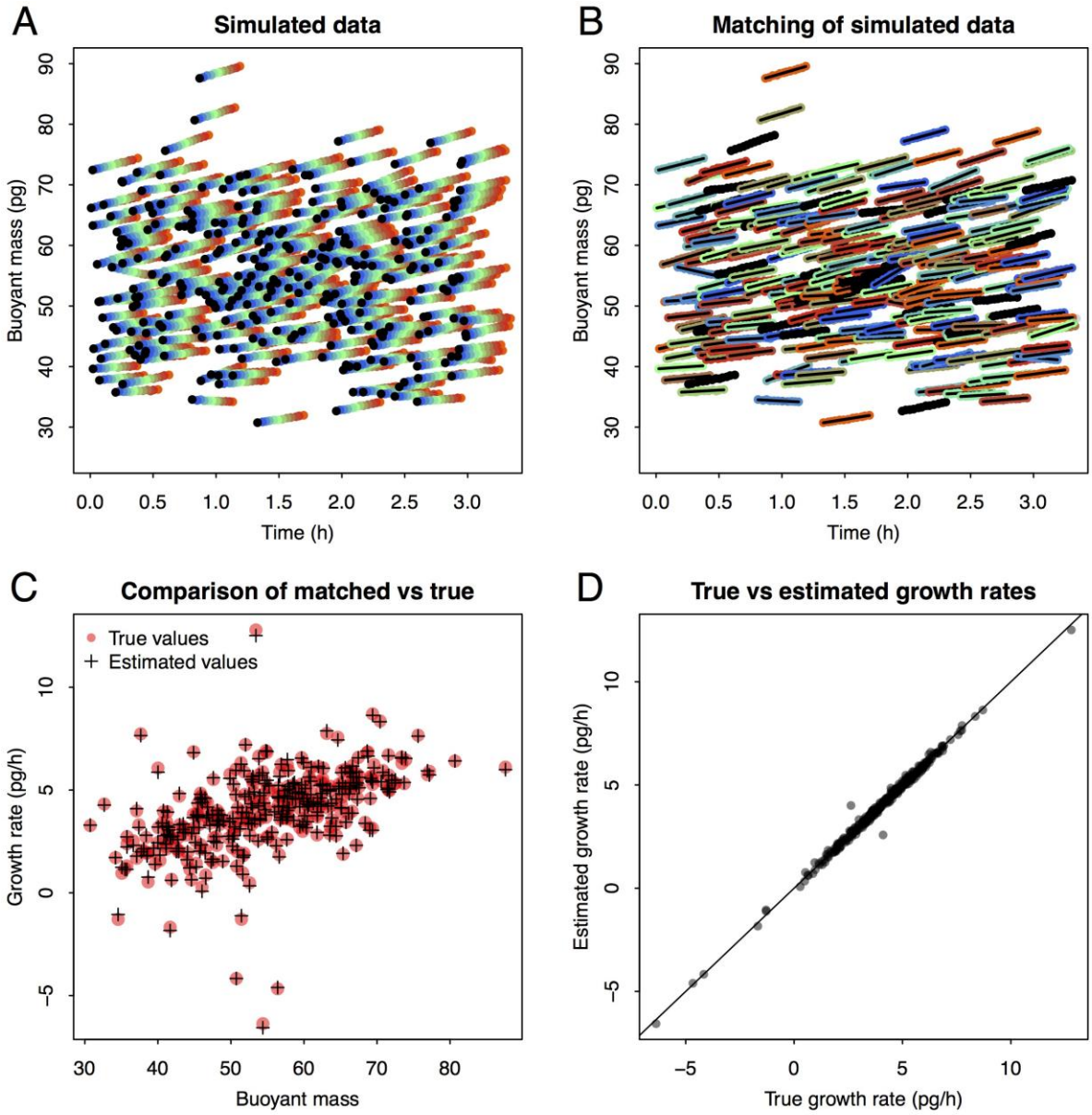

Supplementary Figure 5

Simulation of the cell-matching process.

Simulation of the cell matching process showing that single cells are reliably matched by our method. (A) We simulate a set of cells sampled from a joint distribution of mass and mass accumulation rate similar to the L1210 cells shown in Figure 2. However, we simulate cells entering the serial SMR array at a rate of 100 cells per hour (two-fold more concentrated than we have used in our experiments). Each cell varies in the time it takes to travel from each cantilever to the next (mean 1.9 minutes, standard deviation 0.3 minutes), and Gaussian noise is added to each buoyant mass measurement (standard deviation 0.05 pg, similar to that of our large-channel device). (B) We then match the measurements in the simulated data. All data points that have been matched together as corresponding to the same cell have been colored the same randomly-chosen color. (C) Comparison of the masses and mass accumulation rates from which the data in (A) was generated, and the observed mass and mass accumulation rates, showing excellent agreement. (D) Comparison of mass accumulation rates from which the data in (A) was generated, and the observed mass accumulation rates, showing excellent agreement, except for in the case of two mismatched cells (off-diagonal points) out of 300 in the simulated dataset.

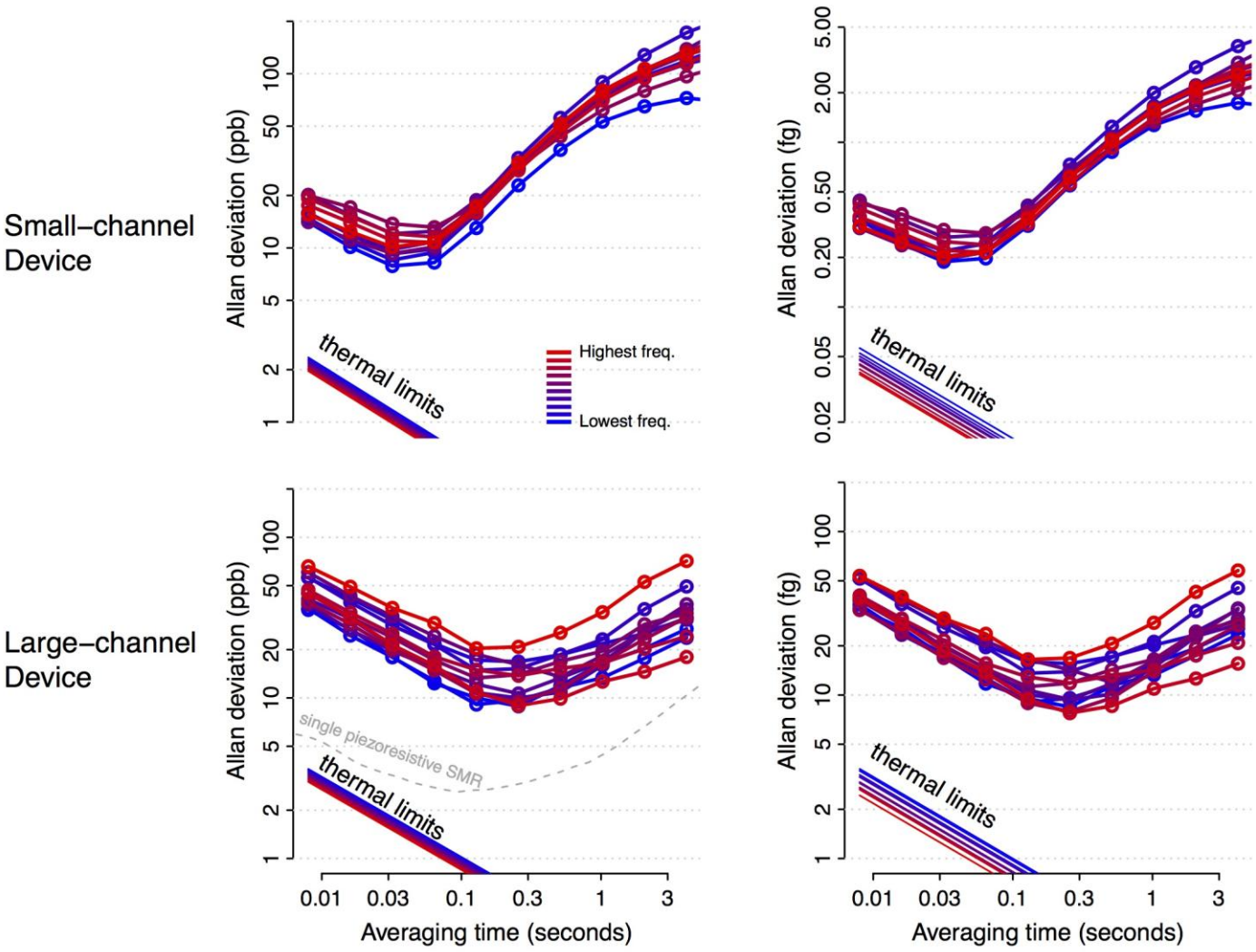

Supplementary Figure 6

Stability of the cantilevers used in the mass sensor arrays.

Measured Allan deviations of all cantilevers on two separate devices. Left two plots show Allan deviations in fractional frequency units, relative to the unloaded cantilever frequency (colored dots/lines). For reference, the dashed grey line indicates the measured noise performance of an optimized piezoresistive single large-channel SMR. Right two plots show Allan deviations rescaled by each cantilever's mass sensitivity. Theoretical thermomechanical limitations on the lowest achievable Allan deviations are also plotted (calculated from [2]), assuming the cantilever is driven to a mean-squared displacement one billion times (90 dB) above the thermally-driven mean-squared displacement. While larger drive amplitudes would theoretically further reduce these limits, mechanical nonlinearity typically becomes significant beyond 90 dB, limiting noise performance.

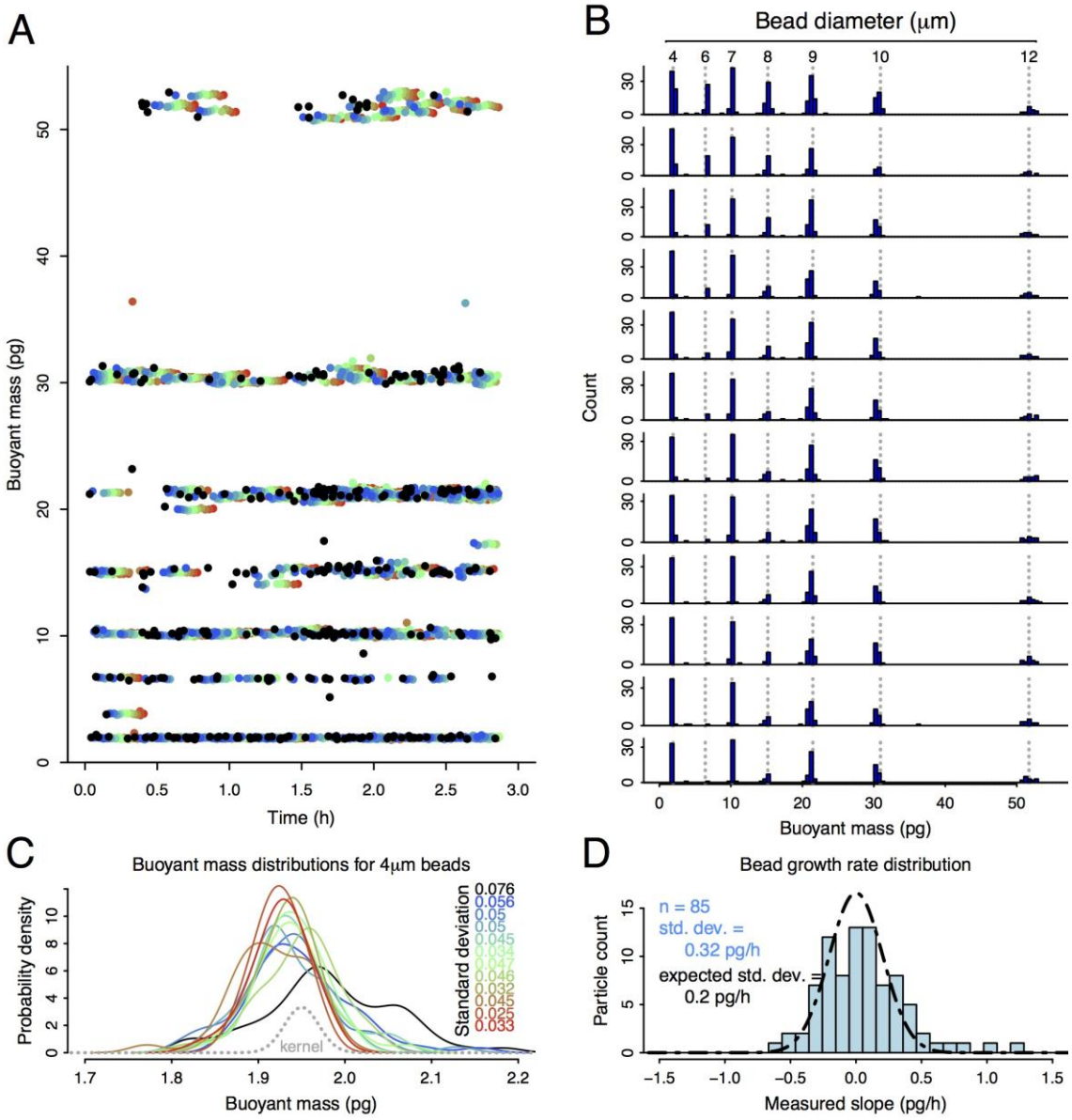

Supplementary Figure 7

Mass accumulation rate resolution of the large-channel devices.

Measuring a mixture of plastic microparticles to determine mass accumulation rate resolution on a large-channel serial mass sensor array. (A) We measured a mixture of 4, 6, 7, 8, 9, 10 and 12 μm polystyrene beads (Duke Standards, NIST traceable, Thermo Scientific) at 37 C in 0.01% Tween-20 in water. Sensors were calibrated by linearly rescaling their raw frequency signals such that the 7 μm bead modal mass is the expected buoyant mass (10.15 pg). (B) Across all sizes and sensors, particle buoyant masses match the expected buoyant masses (dashed lines), verifying that the sensors are linear over this size range. (C) 4 μm particles have the lowest size variability (in pg) of these beads according to manufacturer's datasheet, and therefore their distribution's width is a reasonable upper bound on the sensor error. Typical sensor root-mean-square-error is on the order of 0.05 pg. (D) Histogram of mass accumulation rates (errors, as particles are not growing) of 85 single particles for which at least 10 sensors could be linked together. Mass accumulation rates were calculated excluding data from the first sensor, which displayed much higher noise than the other sensors. Dashed line shows estimated mass accumulation rate distribution assuming t = 1.4 minutes, k = 11, and σ = 0.05 pg, showing good agreement between this approximation for mass accumulation rate error and the observed mass accumulation rate error distribution.

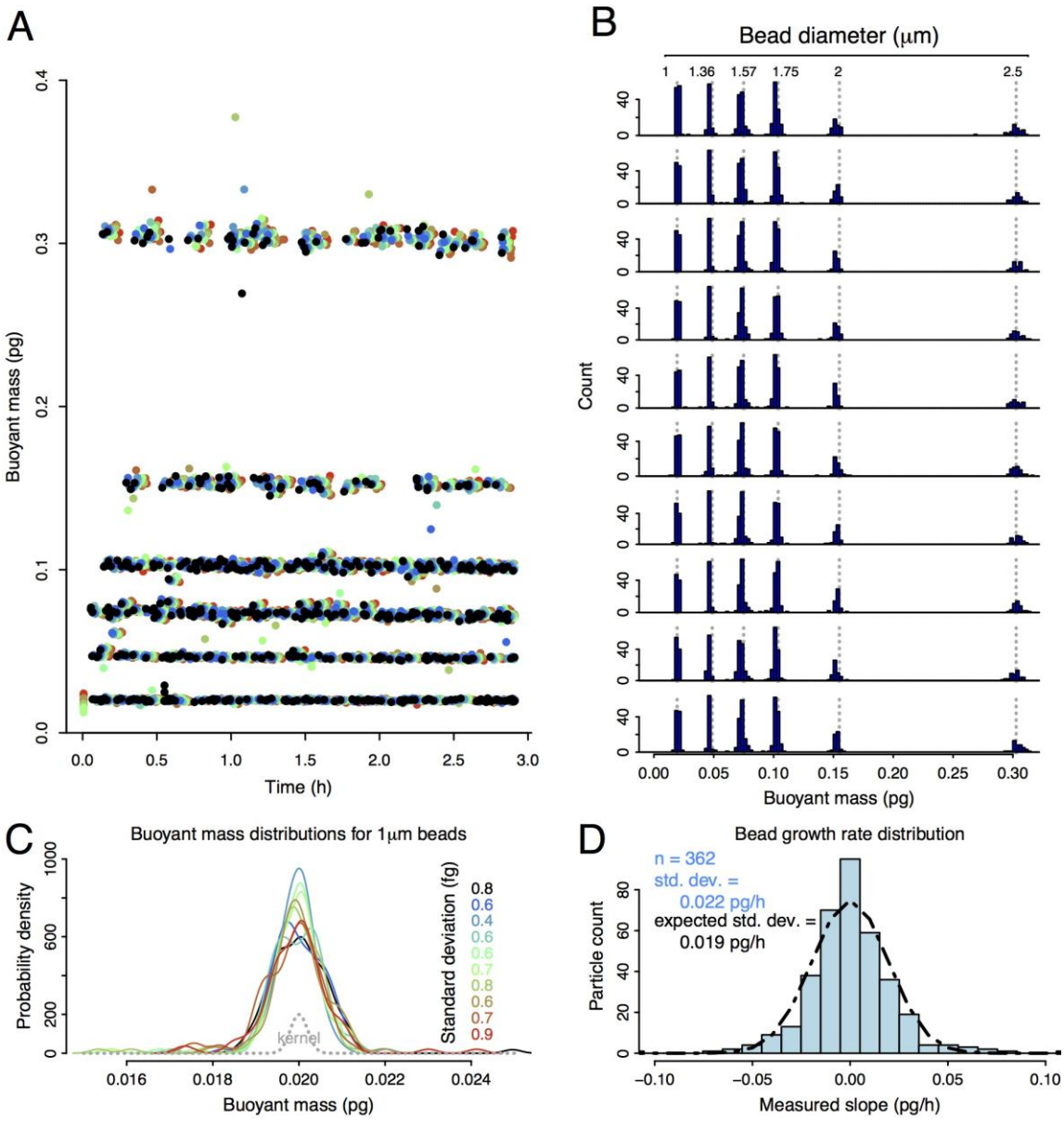

Supplementary Figure 8

Mass accumulation rate resolution of the small-channel devices.

Same as Supplementary Figure 7, but for a small-channel serial SMR array. (A) We measured a mixture of 1.0, 1.36, 1.57, 1.74, 2.0, and 2.5 μm polystyrene beads (Duke Standards, Thermo Scientific, except for 1.0 μm, from Bangs Labs) at 37 C in LB with 0.1% Tween-80. Sensors were calibrated by linearly rescaling their raw frequency signals such that the 1.0 μm bead modal buoyant mass is 0.02 pg (the expected buoyant mass in LB at a density of 1.013 g/mL). (B) Distributions of measured buoyant masses for each SMR in the array, demonstrating both linearity and precision in each cantilever mass measurement. (C) Buoyant mass distributions of 1 μm polystyrene particles provide an upper bound on each cantilever's buoyant mass measurement error, here on the order of 0.5-1 fg. (D) Mass accumulation rate distribution of single 362 single particles, yielding a mass accumulation rate standard error of 0.022 pg/h. Dashed line shows mass accumulation rate distribution based on equation 2 assuming t = 24 seconds, k = 10, and σ = 0.001 pg.

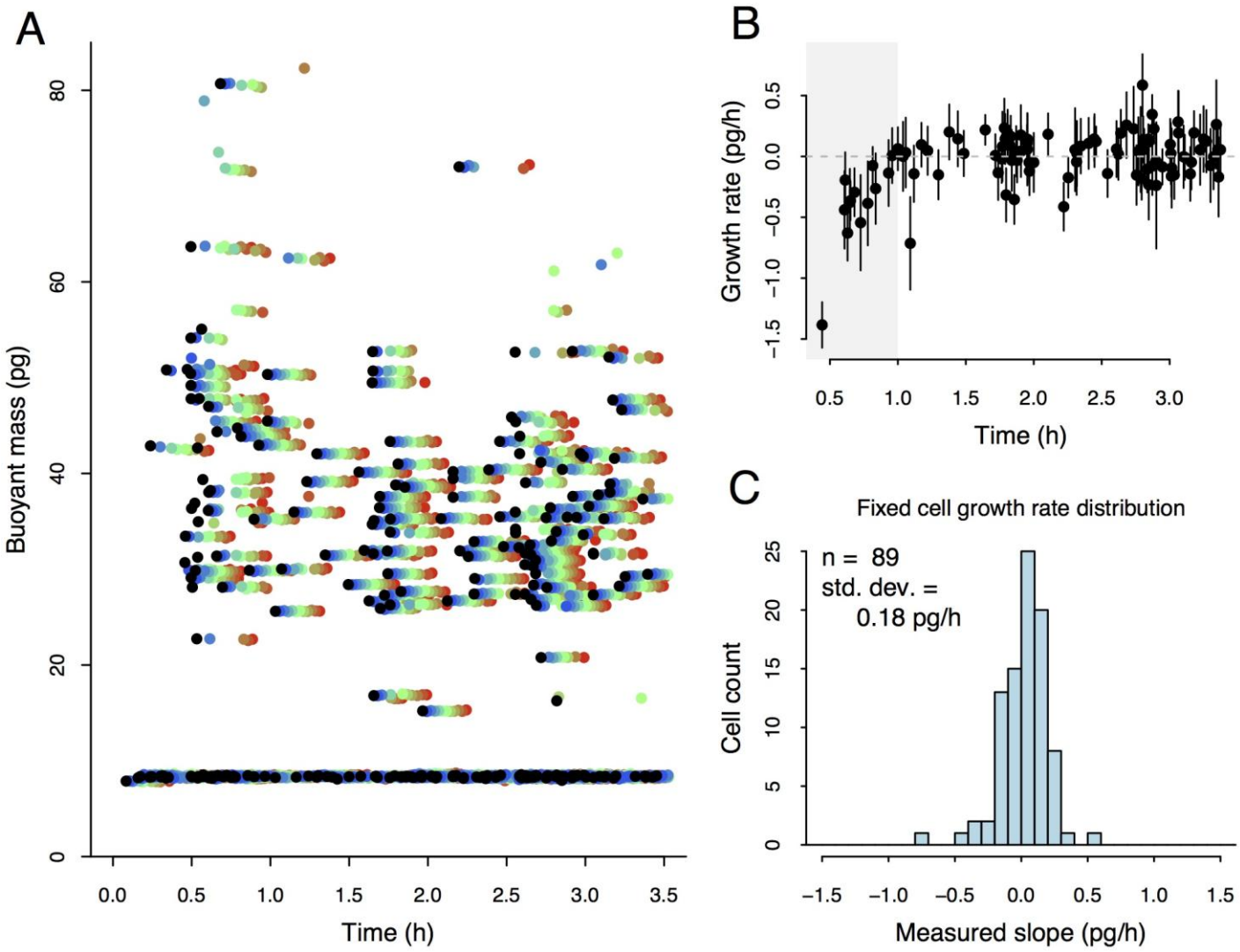

Supplementary Figure 9

Mass accumulation rate of a fixed mouse lymphoblast cell line (L1210).

(A) Buoyant mass trajectories for fixed L1210 cells, measured in phosphate-buffered saline at 37 C. (B) By plotting mass accumulation rate against time, the first cells going through the array can be seen to be losing mass. We believe this is real mass loss attributable to the temperature shift (cells had been fixed and stored at 4 C), and note that after one hour into the measurement cells appear to have equilibrated and no further mass loss occurs. (C) Histogram of mass accumulation rates of fixed cells, excluding the first hour of measurements.

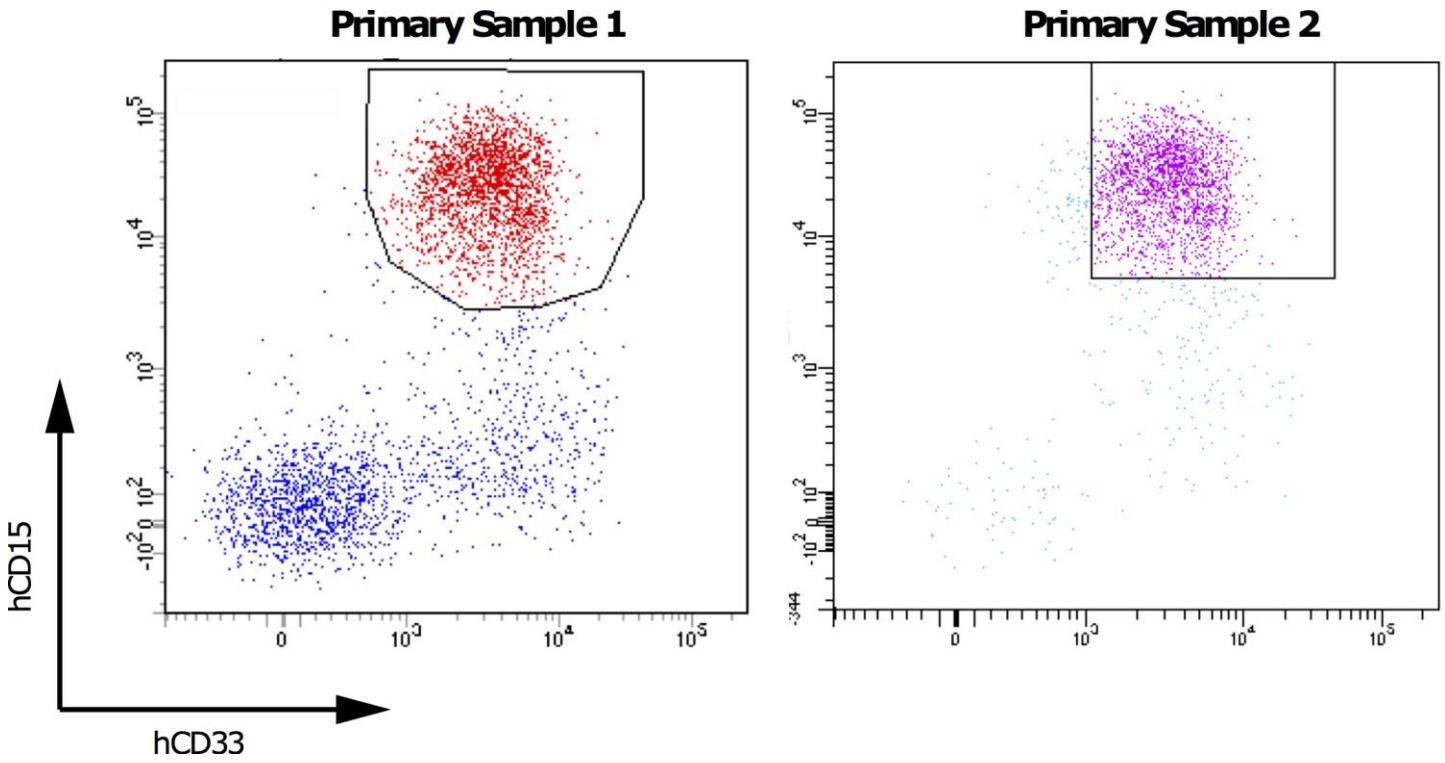

Supplementary Figure 10

FACS plots of primary acute myeloid leukemia cells.

FACS plots of two primary AML samples whose growth properties were assessed on the SMR. Fresh primary peripheral blood or bone marrow samples from patients with newly diagnosed AML were subject to erythrocyte lysis and stained with antibodies targeting human CD33 and human CD15, and leukemia cells were enriched by performing FACS for hCD33/hCD15 double-positive cells. Left panel (sample 1): primary peripheral blood sample from a patient with AML with monocytic differentiation and extensive circulating disease. Contemporaneous clinical testing confirmed that this leukemia expressed CD33 and CD15 and demonstrated that it comprised 43% of peripheral blood mononuclear cells, on which this sample was gated. Of note, this specimen was obtained after the patient had received cytoreductive chemotherapy (hydroxyurea) for three days. Right panel (sample 2): primary bone marrow aspirate from a patient with therapy-related AML. Of note, this specimen did not undergo immunophenotyping by the clinical lab, but morphologic analysis suggested that the leukemia comprised a minority of cells in this double-positive population.

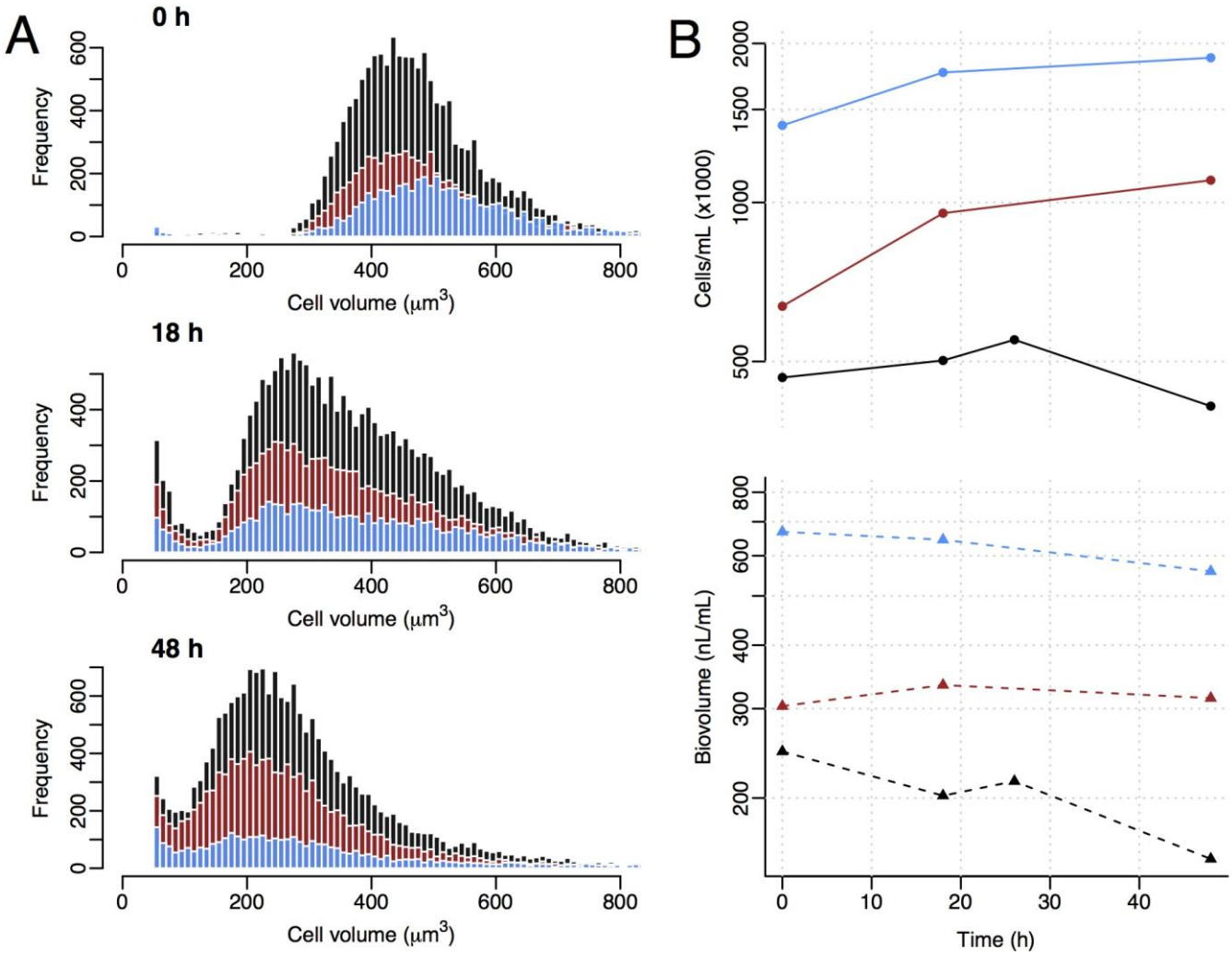

Supplementary Figure 11

Culturing AML cells *ex vivo*.

We seeded cells obtained from Patient 1 (Figure 4 and Supplementary Figure 10) at 0.5, 0.7 and 1.5 million cells/mL (blue, red, and black, respectively) into 6-well culture dishes. (A) We profiled these cultures volume distributions over the next 48 hours with a coulter counter (Beckman Coulter Multisizer 4, 100 μm aperture). The cultures behaved similarly for different inoculation densities. (B) Total cell counts generally increased slightly, but total biovolume decreased.

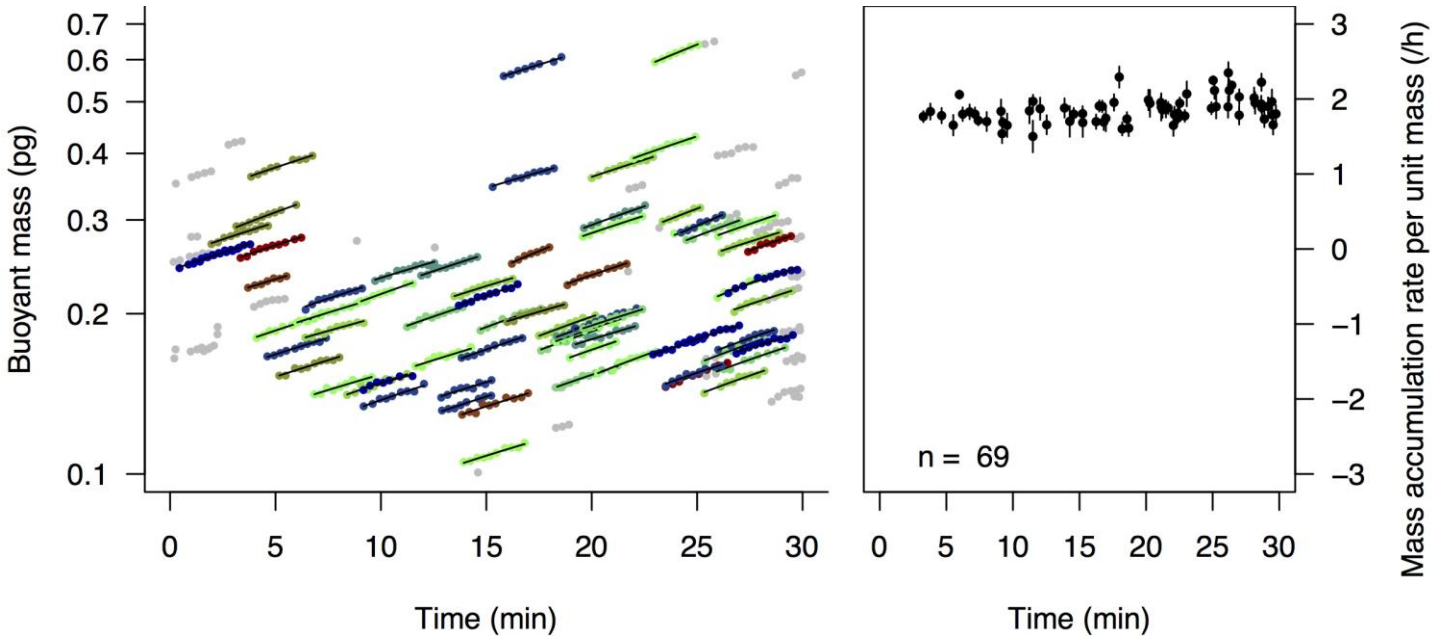

Supplementary Figure 12

Mass accumulation rate of *E. faecalis* measured on a small-channel mass sensor array.

At the left, colored dots show points which were determined to correspond to a single cell, for which the mass accumulation rate was determined and plotted against the cell's mass (right). Grey points indicate measurements for which less than seven mass measurements could be linked together, and were not used in the analysis at right. E. faecalis was grown in Brain-Heart Infusion (BHI, Difco) overnight and transferred to fresh BHI with 0.2% Tween-80 at a 105-fold dilution approximately three hours prior to measurement. 1.36 μm beads were used as the calibration standard and have been omitted from the plot at left for clarity.

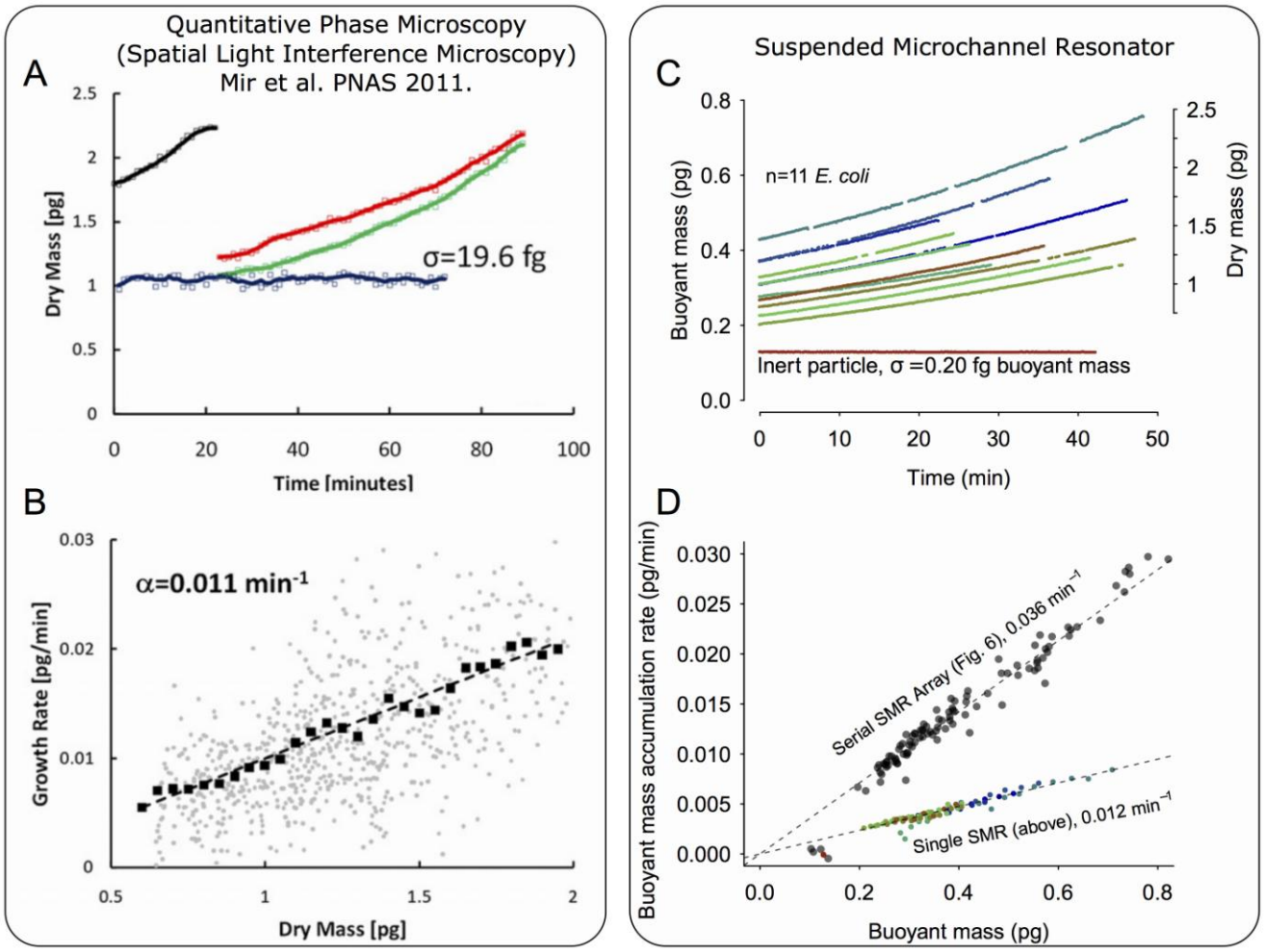

Supplementary Figure 13

Comparison of precision between recent quantitative-phase microscopy measurements and SMR measurements.

Plots in (A) and (B) are excerpted from Mir et al. [3]. Insets in the original figure (A) and caption segment describing the insets have been omitted for clarity. Original caption reads:

> SLIM measurements of E. coli growth. (A) Dry mass vs. time for a cell family. [...] The blue line is a fixed cell measurement, with SD of 19.6 fg. Markers indicate raw data, and solid lines indicate averaged data. (B) Growth rate vs. mass of 20 cells measured in the same manner. Faint circles indicate single data points from individual cell growth curves, dark squares show the average, and the dashed line is a linear fit through the averaged data; the slope of this line, 0.011 min 1, is a measure of the average growth constant for this population. The linear relationship between the growth rate and mass indicates that, on average, E. coli cells exhibit exponential growth behavior.

(C) Single-cell E. coli (ATCC 43893) growth trajectories measured on a single SMR (160 μm long with a 3 by 5 μm interior channel, operated in the second vibrational mode at 1.1 MHz) of similar design to the SMRs in serial SMR arrays. Growth was measured by passing a single cell back and forth through the SMR, as in [4]. Data points from other cells that entered the sensor during the dynamic trap (but were ignored by the trapping algorithm) were removed. SMR measurements were made in LB at room temperature, yielding a similar growth rate as in Mir et al. [3], which used E. coli MG1655 in M9-casamino acid media at 37 C. (D) Colored points are buoyant mass accumulation rates estimated from the data in (C), based on linear fits to non-overlapping 5-minute segments. Five minutes was chosen as that was the width of the applied smoothing filter in (A) and (B). Black points are mass accumulation rates from *E. coli* cells at 37 C measured in the serial SMR array in Figure 6A. Dashed lines show best linear fits in which the intercept was forced to zero, and corresponding exponential growth rates are noted for the two experiments. Note that the terminology of 'growth rate' used in (B) is equivalent to 'mass accumulation rate'.

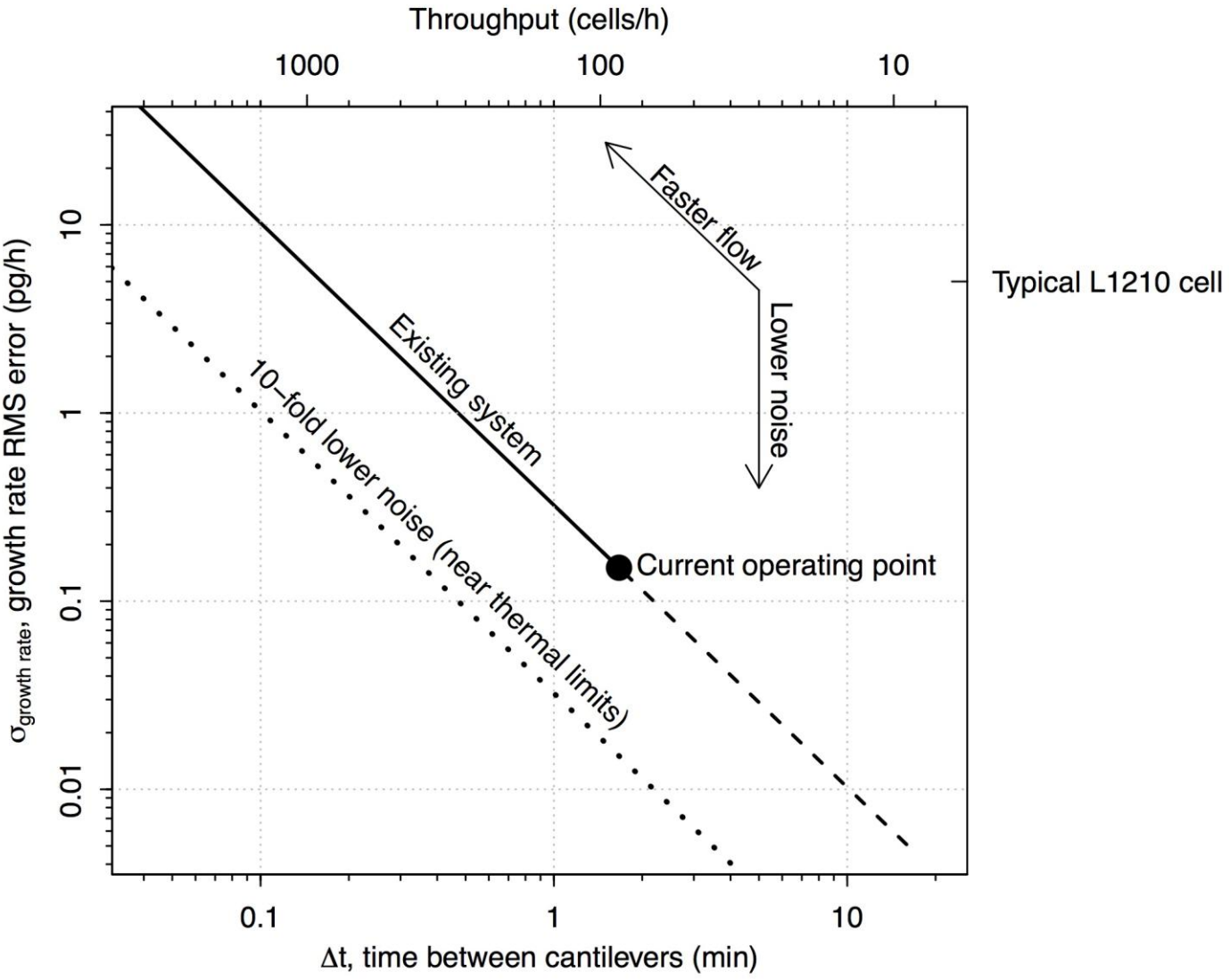

Supplementary Figure 14

Theoretical trade-off between throughput and resolution.

Theoretical trade-off between throughput and resolution for the large-channel devices used in this study, with 12 mass sensors and delay channels with volumes 120-fold higher than the volume of a single cantilever. We assume the cell concentration cannot exceed one cell per 50 sensor volumes (to avoid two cells being in the sensor at the same time), yielding the line of possible operating points.

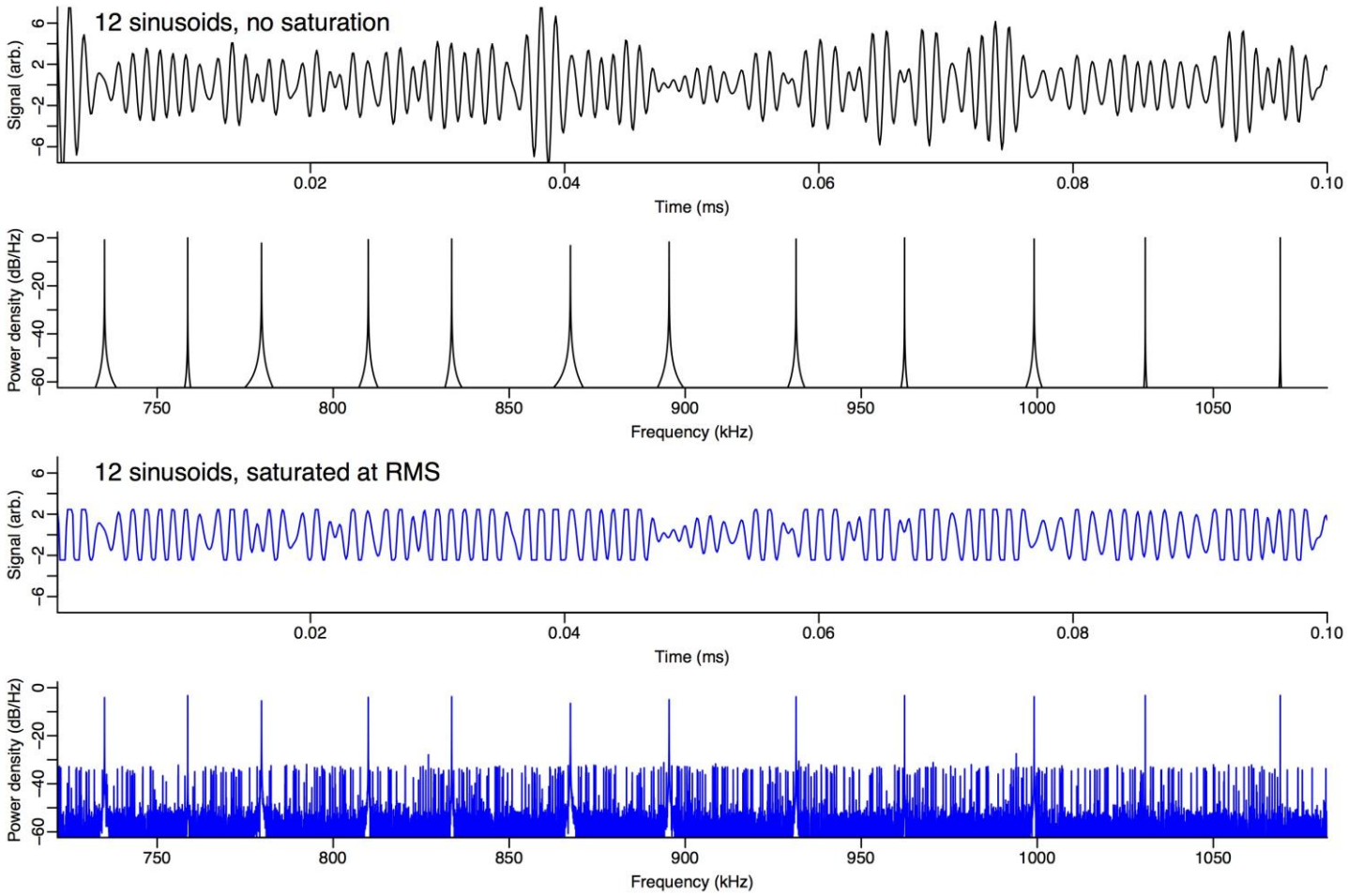

Supplementary Figure 15

Effect of signal clipping in power spectral density around the sensor resonant frequencies.

Saturation applied to a channel carrying many sinusoids adds many other spectral components that are not easily filtered out (noise).

	Primary Sample 1	Primary Sample 2
Patient Characteristics		
Age	82	62
Gender	Male	Female
Tumor Characteristics		
Diagnosis	AML with monocytic differentiation	AML (therapy-related)
Diagnostic tissue	Peripheral blood	Bone marrow
Involvement by Leukemia (%)	43	6
Immunophenotype		
Positive	CD45 (dim), HLA-DR, CD56 (subset), CD13, CD33, CD15, CD14 (variable), CD11b (subset), CD64	N/A
Negative	CD34, CD117	N/A
Karyotype	Normal (46,XY)	46,XX, t(1;16)(p32;p13.1), t(8;21)(q22;q22)
Molecular abnormalities	FLT3, NPM1, TET2 mutations	None detected
Prior AML therapy	Hydroxyurea x 3 days	None

Supplementary Table 1
Clinical characteristics of primary AML samples studied with a serial SMR array.

Note 1: Resolution of mass accumulation rate sensor

How precisely can we measure the mass accumulation rate of a cell? To measure the mass accumulation rate, we will measure the cell size k times, once everyΔ t minutes, and fit a model to explain how it varies over time. Here we will assume the total duration of the measurements ($k\Delta t$) is short enough that a line is an appropriate model. So the problem becomes, how precisely can we know the slope of a line?

Fortunately, least-squares slope estimates can be written as a linear combination of the observed size values, Y, as follows [5]:

$$\begin{bmatrix}\text{intercept}\\ \text{slope}\end{bmatrix} = (X^T X)^{-1} X^T Y$$

Here X is a $k \times 2$ matrix, where the first column is filled with ones, and the second column corresponds to the evenly-spaced times at which the cell size is measured. For simplicity, we assume the times are mean-centered, yielding the following time vector:

$$\begin{bmatrix}\frac{-k+1}{2}\Delta t & \frac{-k+3}{2}\Delta t & \frac{-k+5}{2}\Delta t & \dots & \frac{k-1}{2}\Delta t\end{bmatrix}$$

which we will generally simply denote as $\begin{bmatrix}\frac{-k+1}{2}\Delta t & \dots & \frac{k-1}{2}\Delta t\end{bmatrix}$. Plugging in this definition of X gets us to the coefficient vector relating the measured sizes to the slope estimator (specifically, this coefficient vector is the second row of $(X^T X)^{-1} X^T$).

$$\begin{bmatrix}\text{intercept}\\ \text{slope}\end{bmatrix} = \left(\begin{bmatrix}1 & \dots & 1\\ \frac{-k+1}{2}\Delta t & \dots & \frac{k-1}{2}\Delta t\end{bmatrix} \begin{bmatrix}1 & \frac{-k+1}{2}\Delta t\\ \vdots & \vdots\\ 1 & \frac{k-1}{2}\Delta t\end{bmatrix} \right)^{-1} \begin{bmatrix}1 & \dots & 1\\ \frac{-k+1}{2}\Delta t & \dots & \frac{k-1}{2}\Delta t\end{bmatrix} \begin{bmatrix}y_1\\ \vdots\\ y_k\end{bmatrix} \tag{1}$$

$$\begin{bmatrix}\text{intercept}\\ \text{slope}\end{bmatrix} = \left(\begin{bmatrix}k & 0\\ 0 & \Delta t^2 \frac{k^3-k}{12}\end{bmatrix} \right)^{-1} \begin{bmatrix}1 & \dots & 1\\ \frac{-k+1}{2}\Delta t & \dots & \frac{k-1}{2}\Delta t\end{bmatrix} \begin{bmatrix}y_1\\ \vdots\\ y_k\end{bmatrix}$$

$$\begin{bmatrix}\text{intercept}\\ \text{slope}\end{bmatrix} = \frac{1}{k\Delta t^2 \frac{k^3-k}{12}} \begin{bmatrix}\Delta t^2 \frac{k^3-k}{12} & 0\\ 0 & k\end{bmatrix} \begin{bmatrix}1 & \dots & 1\\ \frac{-k+1}{2}\Delta t & \dots & \frac{k-1}{2}\Delta t\end{bmatrix} \begin{bmatrix}y_1\\ \vdots\\ y_k\end{bmatrix}$$

$$\text{slope} = \frac{k}{k\Delta t^2 \frac{k^3-k}{12}} \begin{bmatrix}\frac{-k+1}{2}\Delta t & \dots & \frac{k-1}{2}\Delta t\end{bmatrix} \begin{bmatrix}y_1\\ \vdots\\ y_k\end{bmatrix}$$

$$\text{slope} = \frac{1}{\Delta t \frac{k^3-k}{12}} \begin{bmatrix}\frac{-k+1}{2} & \dots & \frac{k-1}{2}\end{bmatrix} \begin{bmatrix}y_1\\ \vdots\\ y_k\end{bmatrix}$$

Since the slope estimate is a linear combination of observed size values $Y = [y_1\ y_2\ \dots\ y_k]^T$, errors also propagate linearly. If all the size measurements have independent and identically distributed errors with mean zero and root-mean-square-error (RMSE) σ_ϵ, then the slope RMSE is σ_ϵ times the magnitude of the coefficient vector, $\frac{1}{\Delta t \frac{k^3-k}{12}} \begin{bmatrix}\frac{-k+1}{2} & \dots & \frac{k-1}{2}\end{bmatrix}$. The magnitude of $\begin{bmatrix}\frac{-k+1}{2} & \dots & \frac{k-1}{2}\end{bmatrix}$ is $\sqrt{\frac{k^3-k}{12}}$, therefore

$$\sigma_{\text{slope}} = \frac{\sigma_\epsilon \sqrt{12}}{\Delta t \sqrt{k^3-k}} \approx \frac{\sigma_\epsilon \sqrt{12}}{\Delta t k^{1.5}} \tag{2}$$

It is worth note that we could parameterize this instead in terms of total time transiting the array, $T = k\Delta t$, with k measurements occurring at evenly-spaced increments throughout this interval.

$$\sigma_{\text{slope}} \approx \frac{\sigma_\epsilon \sqrt{12}}{T \sqrt{k}}$$

In this form, it is clearly seen that the standard error scales inversely proportional to the total measurement duration, with a $\sqrt{k}$ dependence on the number of measurements made during that interval (in direct analogy to the central limit theorem).

We can use equation (2) generally to estimate the resolution of any sytem measuring rates of mass or volume increase, but specifically in the case of a serial SMR array, it also provides a convenient way to express the effect of the flow rate, which controls the trade-off between mass accumulation rate resolution and throughput. As we increase the flow rate, we decrease$\Delta\ t$ proportionally, which decreases the mass accumulation rate resolution. Simultaneously, the throughput goes up directly proportionally to flow rate. An added effect is that faster flow rates yield larger *mass* error, σ_ϵ, as the cell spends a smaller amount of time in the cantilever and therefore cannot filter out as much frequency noise. For white-noise-dominated resonant frequency measurements (here corresponding to flow rates faster than what we've utilized in this paper for large-channel devices, e.g.$\Delta\ t < 2$ minutes), we expect that σ_ϵ will scale roughly inversely proportional to the square root of$\Delta\ t$:

$$\sigma_\epsilon = \frac{\alpha}{\sqrt{\Delta t}} \tag{3}$$

Plugging this into (2) suggests that as we increase the flow rate, the mass accumulation rate error is expected to scale with throughput ($1/\Delta t$) to the three-halves.

$$\sigma_{\text{slope}} = \frac{\alpha\sqrt{12}}{\Delta t^{1.5}\sqrt{k^3 - k}} \tag{4}$$

We have illustrated this resolution-noise trade-off in Supplementary Figure 14. For slower flow, σ_ϵ may not be dominated by white frequency noise but instead by flicker (pink) or brown noise, and therefore (3) will sizably underestimate the actual mass noise magnitude.

Note 2: Mass sensitivity scales with frequency$^{3/2}$ for varied cantilever lengths

The cantilever resonant frequency f is given by $f = \frac{1}{2\pi}\sqrt{\frac{k}{m_{\text{eff}}}}$, where k is the spring constant and m_{eff} is the effective mass of the cantilever. m_{eff} is proportional to the cantilever length l [6], and k is proportional to $1/l^3$ [7], therefore $f \propto \frac{1}{l^2}$.

We can similarly determine how the cantilever mass sensitivity [8], s depends on length: $s \propto \frac{f}{m} \propto \frac{1}{l^3}$. Combining these two facts, we find s will be proportional to $f^{3/2}$, when all dimensional parameters other than the length of the cantilever are kept constant.

Note 3: Explanation of peak matching algorithm

We attempt to identify all the peaks (up to twelve, one in each cantilever) that we believe originate from the same cell. To do this, we use a heuristic approach in which we build "cells", collections of peaks that we believe belong to the same cell. At each cantilever in turn, starting at the second cantilever, we try to match the observed peaks at that cantilever with the previously observed cells. To match peaks to their corresponding cells, we define a cost function, detailed below, representing our assumptions about how cells both grow and flow through the device. We then try to find a way of pairing the already-observed cells (from the first n cantilevers) with the peaks observed at cantilever n+1 that minimally violates our expectations. Additionally, we also include the possibility that a cell is not observed at a particular cantilever, possibly due to simultaneously entering the cantilever at the same time as another cell, or adhering to the device walls. We include this possibility by adding fictitious cells ("gaps") such that a previously-observed cell can be assigned to a gap if there are no peaks at sensor n that are likely to originate from that cell. Similarly, a peak in cantilever n+1 can be assigned to a gap if it doesnt appear to clearly appear to correspond to an existing cell.

Pseudo-code for our matching approach is given below (variables are denoted in blue):

```
Initialize each peak in sensor 1 as its own cell, put them all in cellList

For each sensor n in 1:(numberOfSensors-1)
   peaksToBeAssigned = all peaks in sensor n+1

   costs = matrix( number of rows = length(cellList),
                   number of columns = length(peaksToBeAssigned) )
   Pad costs with extra rows and columns for 'unassigned' cells
   Set entries of costs for assigning a cell to 'unassigned' to gapCost
   Set entries of costs for assigning 'unassigned' to 'unassigned' to 0

   For each r in 1:length(cellList)
      For each c in 1:length(peaksToBeAssigned)
         costs[r,c] = -log( P(peaksToBeAssigned[c] | cellList[r]) )

   Find optimal assignment for costs via Hungarian algorithm

   Any peaks in peaksToBeAssigned that were assigned to existing cells in the cellList
   should be concatenated onto the end of their corresponding cell.

   Any entries in peaksToBeAssigned NOT assigned to existing cells are added to the
   cellList as cells containing only one peak.
```

The heart of this approach is how we define a cost function representing our prior assumptions about device behavior (e.g. cells take approximately two minutes to transit from one cantilever to the next, and can't possibly show up at cantilever 2 before appearing at cantilever 1) and cell behavior (over such a short time period, cell mass usually changes roughly linearly, and the rate of change is unlikely to be extremely large). To represent these assumptions, we use a probabilistic model of seeing a peak of a particular mass and time at sensor n+1, given the previous n peaks we've already decided are part of the cell's trajectory. Using the negative log of the probability gives us a cost function for which minimizing the cost corresponds to maximizing the likelihood of the data.

We model the probability of observing a peak of mass m_{n+1} and at time t_{n+1}, conditioned on the peak occurring at sensor n+1 and having observed previous peaks of masses $m_{1:n}$ at times $t_{1:n}$, as follows:

$$P(m_{n+1}, t_{n+1} | m_{1:n}, t_{1:n}) = P(m_{n+1} | t_{n+1}, m_{1:n}, t_{1:n}) P(t_{n+1} | m_{1:n}, t_{1:n})$$

We then assume t_{n+1} depends only on t_n, and is normally distributed with mean $t_n + \mu_{\Delta t}$ and variance $\sigma^2_{\Delta t}$, where $\mu_{\Delta t}$ and $\sigma^2_{\Delta t}$ are specified by the user *a priori*. We further posit that m_{n+1} should be related to t_{n+1} and the previous data via the following relation

$$m_{n+1} = \beta_1 t_{n+1} + \beta_0 + \epsilon$$

where β_1 is a random variable corresponding to the slope implied by the previous datapoints, β_0 is the y-intercept, and ϵ is random instrument noise. If we mean-center the time values ($\sum_{i \in 1:n} t_i = 0$), then β_0 and β_1 become uncorrelated, and we can thus express the mean and variance of m_{n+1} as

$$\mu_{m_{n+1}} = t_{n+1}\mu_{\beta_1} + \mu_{\beta_0}$$
$$\sigma^2_{m_{n+1}} = t^2_{n+1}\sigma^2_{\beta_1} + \sigma^2_{\beta_0} + \sigma^2_\epsilon$$

Furthermore, if β_1, β_0 and ϵ are assumed normal, then m_{n+1} is normally distributed with the above parameters.

While it is straightforward to obtain frequentist estimates of β_1 and $\sigma^2_{\beta_1}$ when we have already seen many datapoints, we cannot estimate these quantities easily with only one or two datapoints. To mitigate this we use Bayesian estimators, which are shaped by a prior distribution when only one or a few datapoints are available, and shaped more by the data when more data becomes available. The conjugate prior for β_1 is normal (assuming the mass sensor error parameter σ_ϵ is already known) and is specified by hyper-parameters $\overline{\mu}_{\beta_1}$ and $\overline{\sigma}^2_{\beta_1}$. The posterior distributions for β_1 is also normal, with variance and mean as follows:

$$\sigma^2_{\beta_1} = \frac{1}{\frac{1}{\overline{\sigma}^2_{\beta_1}} + \frac{t_{1:n} \cdot t_{1:n}}{\sigma^2_\epsilon}}$$

$$\mu_{\beta_1} = \sigma^2_{\beta_1}\left(\frac{\overline{\mu}_{\beta_1}}{\overline{\sigma}^2_{\beta_1}} + \frac{t_{1:n} \cdot m_{1:n}}{\sigma^2_\epsilon}\right)$$

We also assume that since σ_ϵ is known, μ_{β_0} is just the mean mass from the n previous observations, and $\sigma^2_{\beta_0} = \sigma^2_\epsilon / n$. Using these parameters, we can then write the cost function as:

$$\text{Cost}(m_{n+1}, t_{n+1} | m_{1:n}, t_{1:n}) = -\log\left[N(m_{n+1}|\mu_{m_{n+1}}, \sigma^2_{m_{n+1}})\right] - \log\left[N(t_{n+1}|t_n + \mu_{\Delta t}, \sigma^2_{\Delta t})\right] \quad (5)$$

where $N(x|\mu,\sigma^2)$ is the normal density function evaluated at x with mean μ and variance σ^2. Examples of this cost function for simulated cells are shown in Supplementary Figure 4, demonstrating how this cost function narrows as more and more data is observed.

In sum, the cost depends on the new data (m_{n+1}, t_{n+1}), the previously observed data ($m_{1:n}$, $t_{1:n}$), and five user-defined parameters:

parameter	description
σ	sensor RMS error
$\overline{\mu}_{\beta_1}$	prior expectation for mean mass accumulation rate
$\overline{\sigma}^2_{\beta_1}$	prior expectation for mass accumulation rate variance
$\mu_{\Delta t}$	expected average time between sensors
$\sigma^2_{\Delta t}$	expected variance in time between sensors

Additionally, there is one more parameter for the cost of a gap, yielding six parameters in total controlling the matching process.

It is worth note that by simply choosing the best matching between the previously-observed cells and the newly-observed peaks at every step, we do not properly take into account uncertainty in the matching process. While we have not undertaken this task here, future work to do so may utilize Murty's algorithm [9] to obtain not only the optimal assignment (as provided by the Hungarian algorithm), but a ranked set of the best assignments (e.g. the top 50 assignments). This would allow one to check which assignments are tenuous and which are very certain.

Note 4: Comparison of measurement precision between SMRs and quantitative phase microscopy (QPM)

Comparisons of SMR and QPM mass measurements cannot be made directly because the two methods exploit different physical principles. QPM requires computing an unwrapped phase shift function from image data to yield optical thickness. Optical thickness is integrated over the area of a cell, and the result is multiplied by a constant to convert it into dry mass units. The constant is based on an average refractive increment of mostly globular proteins [10]. On the other hand, SMR measurements are based on the change in resonant frequency of an oscillating cantilever caused by a cell passing through an embedded microfluidic channel. The frequency shift is divided by a sensitivity constant (Hz/pg) to obtain buoyant mass. The sensitivity constant is a device parameter and independent of the properties of the analytes. It is obtained by direct calibration with particles of known buoyant mass.

Supplementary Figures 13A and 13C show mass measurements of *E.coli* cells with similar interdivision times made by QPM (left panel) and SMR (right panel). The left panel shows dry mass versus time for three *E. coli* cells measured by Mir et al. using QPM [3]. Buoyant mass versus time for 11 *E. coli* cells measured by SMR is shown on the right. Buoyant mass error for these cells is 0.22 fg, based on repeat measurements of a single inert polystyrene particle similar in size and density to these cells (1.36 μm diameter, 1.05 g/mL). One way to compare the precision of the two methods is to convert the SMR buoyant mass to dry mass. This is possible using a method we validated in a previous study [11]. Briefly, we measured the buoyant mass of *E. coli* cells in two fluids with different densities. The first fluid was a standard phosphate-buffered saline solution. The second fluid was identical to the first, except the water in the formula was replaced by heavy water (D_2O). Using the method of Archimedes, we found the density of *E. coli* biomass (*E. coli*'s dry density) to be 1.45 g/mL. This constant can be used to convert buoyant mass to dry mass, as shown on the right axis in Supplementary Figure 13C. The conversion produces good agreement between the *E. coli* dry mass obtained by the two methods. Converting buoyant mass error to dry mass error yields an error of 0.63 fg, approximately 30 times smaller than values produced by QPM.

Another way to assess the precision of the two methods is to compare the relative uncertainties of both techniques. Because they are unitless, relative uncertainties can be compared directly. In Mir et al. [3], measurements of a $\sim$1.5 pg cell dry mass have a standard deviation of $\sim$0.0196 pg, yielding a relative uncertainty of 1.3%. SMR measurements of similarly-sized cells with an average buoyant mass around 0.3 pg have a standard deviation of 0.20 fg, or 0.06% relative uncertainty, about 20 times better precision than QPM. Both the dry mass conversion and relative uncertainty approaches give similar values.

We also find that serial and single SMR measurements of mass accumulation rates exhibit less variation than those measured by QPM. Supplementary Figures 13B and 13D compare mass accumulation rate measurements obtained by QPM and SMR. The left panel (Supplementary Figure 13B) shows dry mass accumulation rate (referred to as growth rate) vs. dry mass of 20 cells measured in reference [3]. Supplementary Figure 13D shows two analogous datasets produced by the SMR method - one taken with a single SMR device at low throughput and another taken on a serial SMR array with a higher flow rate.

How does the noise of the single SMR compare to the serial SMR array results shown in Figure 6 and Supplementary Figure 13? The uncertainty in SMR buoyant mass measurements depends on the flow rate of cells through the device. By varying the flow rate, the system can be optimized for throughput or measurement precision. The noise level in the serial SMR array measurements (Figure 6) is about 3 times higher than the single SMR in Supplementary Figure 13C because of the faster flow rate. This could be reduced at the expense of lower throughput.

References

[1] S. Olcum, N. Cermak, S. C. Wasserman, and S. R. Manalis, "High-speed multiple-mode mass-sensing resolves dynamic nanoscale mass distributions," *Nat Commun*, vol. 6, May 2015.

[2] E. Gavartin, P. Verlot, and T. J. Kippenberg, "Stabilization of a linear nanomechanical oscillator to its thermodynamic limit," *Nat Commun*, vol. 4, Dec. 2013.

[3] M. Mir, Z. Wang, Z. Shen, M. Bednarz, R. Bashir, I. Golding, S. G. Prasanth, and G. Popescu, "Optical measurement of cycle-dependent cell growth," *Proc Natl Acad Sci USA*, vol. 108, pp. 13124–13129, Aug. 2011.

[4] M. Godin, F. F. Delgado, S. Son, W. H. Grover, A. K. Bryan, A. Tzur, P. Jorgensen, K. Payer, A. D. Grossman, M. W. Kirschner, and S. R. Manalis, "Using buoyant mass to measure the growth of single cells," *Nat Meth*, vol. 7, pp. 387–390, Apr. 2010.

[5] D. Wackerly, W. Mendenhall, and R. L. Scheaffer, *Mathematical Statistics with Applications*. Belmont, CA: Thomson Brooks/Cole, 7 ed., 2008.

[6] A. Cleland, *Foundations of Nanomechanics: From Solid-State Theory to Device Applications*. Advanced Texts in Physics, Springer Berlin Heidelberg, 2002.

[7] S. P. Timoshenko and J. M. Gere, *Mechanics of Materials*. New York: Van Nostrand Reinhold Co., 1 ed., 1972.

[8] K. L. Ekinci, Y. T. Yang, and M. L. Roukes, "Ultimate limits to inertial mass sensing based upon nanoelectromechanical systems," vol. 95, no. 5, pp. 2682–2689.

[9] K. G. Murty, "Letter to the Editor - An Algorithm for Ranking all the Assignments in Order of Increasing Cost," *Operations Research*, vol. 16, pp. 682–687, June 1968.

[10] R. Barer, "Refractometry and Interferometry of Living Cells," *J. Opt. Soc. Am.*, vol. 47, pp. 545–556, June 1957.

[11] F. Feijó Delgado, N. Cermak, V. C. Hecht, S. Son, Y. Li, S. M. Knudsen, S. Olcum, J. M. Higgins, J. Chen, W. H. Grover, and S. R. Manalis, "Intracellular water exchange for measuring the dry mass, water mass and changes in chemical composition of living cells," *PLoS ONE*, vol. 8, no. 7, p. e67590, 2013.